Coronal Currents, Magnetic Fields and Heating in a Solar Active Region

Jeongwoo Lee
Astronomy Department, University of Maryland, College Park, MD 20742

A. N. McClymont
Institute for Astronomy, University of Hawaii, Honolulu, HI 96822

Zoran Mikić
Science Applications International Corporation, San Diego, CA 92121

Stephen M. White and M. R. Kundu
Astronomy Department, University of Maryland, College Park, MD 20742

Abstract. We compare microwave images of a solar active region with state-of-the-art fully-nonlinear force-free extrapolations of the photospheric fields in order to study the link between coronal currents and heating of the corona. This extrapolation fully takes into account the nonuniform distribution of electric currents observed in the photosphere and its role in the coronal magnetic structure. We carry out the comparison for AR 6615, a complex region observed with the VLA on 1991 May 7. Under the assumption that the microwave emission is dominated by optically thick gyroresonance radiation, we may use the radio images to infer the temperature of the corona at different heights and locations. This is then compared with heating models based on the observed current distribution. We are able to reproduce the radio images remarkably well with a model in which temperature is structured along magnetic field lines, depends on the current on the field line, and increases with height in a manner similar to that inferred from static heated loop models. This result implies a direct link between electric currents and coronal heating.

Key words: Sun: corona — Sun: magnetic fields — Sun: radio radiation

1. INTRODUCTION

One of the goals of radio observations of solar active regions is the elucidation of the coronal magnetic structure. The opacity at microwave frequencies is dominated by the gyroresonance mechanism and thus radio observations are directly sensitive to the coronal magnetic field (e.g., Alissandrakis and Kundu, 1984). However, at present only a limited amount of information on the magnetic field can be extracted due to the limitations of available telescopes. For example, Gary and Hurford (1994) are able to derive the magnetic field strength distribution at the base of the corona by measuring the frequency at which microwave intensity drops from coronal to chromospheric temperatures. When the spectral resolution of the observations is poor, the known relationship between specific microwave frequencies and coronal magnetic field strengths can be exploited (e.g., Schmelz et al., 1995, 1992; Brosius et al., 1992; Nitta et al., 1991). It then becomes necessary to know the coronal height of each frequency in order to locate the inferred field strength. Aschwanden et al.'s (1995) stereoscopic method addresses this problem, under the assumption that the fields do not vary with time. In other analyses, model calculations of the theoretical radio brightness are made by adopting a plausible magnetic field model and comparing this with the data. Numerous works exist in this category; we refer to White and Kundu (1997) for a review. Recent works that were not included therein include Gopalswamy et al. (1996), Nindos et al. (1996), Brosius et al. (1996), and Vourlidas, Bastian, and Aschwanden (1997). Both approaches have contributed to our knowledge of active region structure, each with their own advantages. Note, however, that both these techniques primarily focus on obtaining coronal magnetic field strengths.

There is another class of approach which we distinguish from the above-mentioned works in that it more explicitly addresses the vector nature of the magnetic fields of solar active regions. By "vector nature" we mean the connectivity of the lines of force. This will be important if the coronal temperature is structured along field lines, as is widely assumed when the temperature structure of the corona is modelled (e.g., Rosner, Tucker, and Vaiana, 1978; Craig, McClymont, and Underwood, 1978). Only two papers have so far used this approach: Schmahl et al. (1982) modelled radio emission from an arcade of magnetic field lines using a linear force-free field extrapolation in which the parameter α relating the current density $\mathbf{J}$ and magnetic field $\mathbf{B}$ is constant throughout the volume of the active region. They found that the direction of the elongation of the main bulk of the gyroemission itself strongly limits the possible choice of α. Chiuderi-Drago, Alissandrakis, and Hagyard (1987) studied a magnetic field structure connecting two spots and calculated the electron temperature under the assumption that energy transfer occurs mainly along individual field lines. According to these works, the active region temperature structure is not separate from, but rather is closely related to, that of magnetic field lines, so that information on both quantities can be derived from radio observations in a consistent manner.

This paper constitutes a third effort to incorporate the vector nature of the coronal magnetic field into an analysis of radio data. We analyze a well-observed complex and vigorously-heated active region, and go beyond the step of a consistency check between the coronal field extrapolation and the observed radio images. Here we test whether a coronal heating model based only on observations and on the assumption that temperature in the corona is structured along field lines can reproduce, in detail, the microwave images. Since coronal currents necessarily influence the connectivity of coronal magnetic fields as well as their strengths, we use a state-of-the-art nonlinear force-free-field (FFF) extrapolation of the photospheric vector magnetic field (McClymont, Jiao, and Mikić, 1997) in order to account fully for the actual nonuniform distribution of currents in the active region. We then investigate the role of currents in coronal heating as well.

2. RADIO DATA vs. Hα AND CONTINUUM IMAGES

The target of the present study is AR 6615 which was observed on 1991 May 7 at S07 W30. This active region was complex enough and possessed sufficiently powerful currents to make it an excellent candidate in which to explore field line connectivity. Further, heating seems to have been particularly strong in this region since AR 6615 shows perhaps the highest quiescent brightness temperatures of any active region observed so far with the VLA. The role of the currents in enhancing the coronal magnetic field strength above the values suggested by a current-free extrapolation of surface fields have been discussed by Lee et al. (1997).

In Figure 1 we compare the radio and optical images of the region. The upper panels of Figure 1 show optical continuum and Hα line–center images obtained with the Multichannel Double Pass spectrograph (Mein, 1991; Mein et al. 1993) installed on the German Vacuum Tower Telescope at Teide Observatory on Tenerife (provided by Dr. B. Schmieder). The continuum image shows six distinct spots, which we label S1–S6. S1, S2, and S3 are of positive magnetic polarity while S4, S5, and S6 are of negative polarity (this may be seen clearly in the longitudinal magnetogram in Fig. 2). The positions of sunspots are indicated on the other frames of Figure 1 with cross symbols. The Hα image is known to trace magnetic field lines in the chromosphere (Zirin, 1988). The Hα image in Figure 1 therefore suggests that field lines connect S1 to S4 and S5 to S2 and S3, and we indicate these connections by dashed lines in the figure.

We show total radio intensities in the lower panels of Figure 1. The data were obtained using the VLA, and the details of the analysis are discussed by Lee et al. (1997). The spatial resolution is $8.0'' \times 8.0''$ in the 4.9 GHz images and $4.0'' \times 4.0''$ at 8.4 GHz. The radio intensity at 4.9 GHz exhibits two broad peaks (C1 and C2) which are at positions well away from the sunspots and much closer to the magnetic neutral lines between S1 and S4 and between S2, S3 and S5. The 8.4 GHz map is similar to the 4.9 GHz map in overall shape, but slightly different in terms of morphology and the positions of intensity maxima. We label the three main peaks at 8.4 GHz by X1–X3. C1 and X1 are similar in shape but slightly different in position, while C2 and X2–X3 differ in position and morphology. The high electron temperatures inferred from these images (4.4×10^6 K at 4.9 GHz and 4.6×10^6 K at 8.4 GHz in the total intensity images) and the high degrees of circular polarization (see Lee et al., 1997) both indicate that gyroresonance emission in strong coronal fields is the dominant emission mechanism (Zheleznyakov, 1962), and we use this assumption as the basis of our analysis.

All the radio peaks (C1, C2, X1, X2, X3) are located between sunspots, suggesting that they lie at the apexes of field lines connecting sunspots. We note that the 8.4 GHz image resembles the Hα image in that a hot patch connects S2 and S3, elongated E-W. Since we expect the 8.4 GHz emission to arise low in the corona, relatively close to the chromosphere, the similarity between the 8.4 GHz and Hα images suggests that the radio morphology too is determined by the field line connectivity. The 4.9

GHz image is not very similar to the Hα image, which is to be expected since the 4.9 GHz waves are emitted higher in the high corona where the field line structure can be quite different from that in the chromosphere. Therefore, the change of field line connectivity with height in this active region must be addressed in modeling the radio images.

3. MODELING THE RADIO EMISSIONS

The radio intensity at a given frequency, ν, is obtained by integrating the radiative transfer equation. For gyroresonance radiation, which arises from a small number of discrete harmonic layers, this reduces to a simple recurrence relation for the brightness temperature $T_B(\nu)$ such as:

$$T_B(\vec{x}_n, \nu) = T_B(\vec{x}_{n-1}, \nu)e^{-\tau_n(\nu)} + T_e(\vec{x}_n)\Big[1 - e^{-\tau_n(\nu)}\Big]. \tag{1}$$

where T_e and $\tau_n(\nu)$ are the electron temperature and gyroresonant opacity at the nth individual harmonic layer, $\vec{x}_n$. Here the iteration over successive n stops at a harmonic sufficiently high that there is no significant opacity at any higher harmonic–usually above $n = 5$ the opacity is negligible. The expression for gyroresonant opacity has been derived in many places (Zheleznyakov, 1962; Melrose, 1980; Robinson and Melrose, 1984). To quote them, it is in the form:

$$\tau_n(\nu) = .0133 \frac{n_e L_B}{\nu} \frac{n^2}{n!} \Big(\frac{n^2 \sin^2\theta}{2\mu}\Big)^{n-1} F(\theta) \tag{2}$$

where θ is the angle between the magnetic field and the line of sight; n_e is electron density; $\mu = m_e c^2/k_B T_e$; L_B is the magnetic scale length defined by $L_B = B \cdot |\partial B/\partial z|^{-1}$ with z, the distance measured along the line of sight. $F(\theta)$ is a function that depends on the angle, θ, the harmonic, n, and the polaraization state (see White and Kundu (1997) for details).

Thus, calculation of the radio intensity requires magnetic field vectors, temperature and density to be specified in 3-D space. We will describe these model quantities in the next two sections.

4. THE CORONAL MAGNETIC FIELD MODELS

We obtain such a 3-D magnetic field model by extrapolating the photospheric fields into the corona using a vector magnetogram obtained from the Haleakala Stokes polarimeter at Mees Solar Observatory at 17:20 UT as the boundary condition. Figure 2 shows the magnetogram with the longitudinal fields in contours and transverse fields in arrows. The so-called 180-degree ambiguity has been removed using the algorithm of Metcalf (1994). The vector magnetic fields are then coordinate–transformed to the sunspot frame where the nonlinear force–free magnetic field extrapolation (FFF), including the role of currents, is performed using the evolutionary method (Mikić and McClymont, 1994). For comparison we have also calculated a potential–field configuration (PF) in which currents are neglected.

In Figure 3 we show the field line morphologies resulting from the two extrapolations. On comparison of the two models it is immediately found that the active region can be divided into two distinct regions: the eastern part (region A) where the fields are potential-like (i.e., there is essentially no difference between the FFF and PF configurations) and the western part (region B), where the FFF field lines are very different from the PF field lines. This distinction is of course due to the concentration of strong electric currents around spots S2-S3 and S5 (see Fig. 2) which leads to a clockwise twist of the low-lying field lines originating in S5 such that they run nearly parallel to the magnetic neural line which here runs nearly E-W. At greater heights the orientation of the field lines connecting S5 and S2–S3 changes to N-S. The field line configuration predicted by the FFF model is supported by the Hα line–center image of this active region (Figure 1), while the PF model is clearly incompatible with the Hα observation.

We proceed by evaluating the magnetic quantities $(\sin^2\theta, L_B, h_n)$ needed for calculation of the gyroresonant opacity (eq. [2]) from the magnetic field models. Note that at a given frequency these quantities need only be evaluated in the discrete gyroresonant layers because only they contribute to the opacity. It is thus useful to determine the height, h_n, of the gyroresonant layers in each model. We evaluate these quantities at all harmonics from 1 to 5. For illustration purpose, however, we primarily take a look at the results evaluated on the 4th harmonic layers. (As discussed by Lee et al. (1997), the electron temperature in this region was so high that depending on position, it can be optically-thick up to the 4th harmonic.)

We show, in Figure 4, $(\sin^2\theta, L_B, h_n)$ evaluated at two selected isogauss surfaces at 430 G and 750 G which correspond to the fourth harmonics for 4.9 GHz and 8.4 GHz, respectively. The first column shows the height of the isogauss surface above the photosphere, i.e., $h_n(x,y) = (x^2+y^2+z_n^2(x,y))^{1/2} - R_\odot$. Here (x,y) refers to the projected sky plane and z_n is the location of the isogauss surface along the line of sight. The second and the third columns show the emission angle, $\sin^2\theta(x,y,z_n)$ (recall that for gyroresonant emission at the 4th harmonic, the opacity $\propto \sin^6\theta$), and the magnetic length scale, $L_B(x,y,z_n)$, respectively. The solid contours and shading refer to the FFF while the dotted contours show the corresponding quantities in the PF model; each contour is in 10% interval of the maximum value.

The maximum height of 430 G surface is 1.77×10^4 km in the FFF and 1.58×10^4 km in the PF; that of the 750 G surface is 0.92×10^4 km in the FFF and 0.88×10^4 km in the PF. The location of the maximum height in the FFF differs from that of the PF because the PF simply predicts that the strongest magnetic fields lie right above the strongest spot, S4, whereas the FFF model predicts that magnetic flux from S4 is shifted northward and accordingly the local peak of the isogauss surface lies between S4 and S2-S3. The angular term, $\sin^2\theta$ (the second column of Fig. 4: the display range is 0.0 to 1.0), can be of order unity above the photospheric neutral line, but is greatly reduced where the fields are roughly vertical in the sunspot umbrae. Because of the strong angular dependence of gyroemission, it is therefore expected that midway between two spots of opposite polarities will be the favorable place for emission, rather than above the sunspot umbrae (see Figure 1 and Section 2). The magnetic scale length, L_B (the third column), varies by about $\pm 50\%$ within a given surface. Median values of L_B at the 430 G surface are 1.60×10^4 km in the FFF and 1.47×10^4 km in the PF; at the 750 G surface, 1.31×10^4 km in the FFF and 1.28×10^4 km in the PF. Thus the variation of L_B either in a given surface or from model to model is of order of a factor of 2 and therefore plays only a minor role in the variation of opacity.

To summarize, the FFF predicts stronger fields in region B, which leads to a larger magnetic scale length and a wider band of high emission angles (large $\sin\theta$) above the magnetic neutral line. Between regions A and B, the FFF model actually predicts more depressed isogauss surfaces than the PF, since the current-carrying field lines diverge away from the potential-like fields in region A to leave a more field–deficient region between A and B. As expected, the FFF shows little difference from the PF in region A where currents are relatively weak.

5. CORONAL TEMPERATURE MODELS

As mentioned in Section 1, the 3-D temperature structure is crucial for modelling of gyroresonant emission. In most previous studies plane-parallel temperature models have been used, with the exception of Chiuderi-Drago, Alissandrakis, and Hagyard (1987) where temperature modelling was done by solving a heat transfer equation along each field line using the same boundary condition for all field lines. In this study, we adopt a "field line–structured temperature model" (FLST), by which we mean that the temperature in the corona at a given point "knows" about the temperature elsewhere on the same field line, but need not be correlated with the temperature on adjacent field lines (Rosner, Tucker, and Vaiana, 1978; Craig, McClymont, and Underwood, 1978). The underlying physics which motivates such a model is the fact that heat conduction along field lines in the solar corona is very rapid, whereas heat conduction across field lines is very slow. Thus heat which is deposited somewhere on a field line should rapidly be shared with the whole length of the field line.

The FLST is obviously a more realistic approximation to the real corona than a plane parallel model and is commonly adopted in the interpretations of soft X ray and EUV images (e.g., Golub, 1996). The comparison of an FLST model with microwave images is, however, necessarily different in nature from the comparison with soft X-ray images. Whereas soft X-ray intensity is determined by the integration of temperature and emission measure along the line of sight, gyroresonance emission originates from physically thin and often optically thick isogauss surfaces rather than individual field lines, and the observed radio intensity map actually represents the electron temperature distribution. Therefore comparison of radio data with an FLST model requires that we find a prescription for the temperature of a given field line such that the model reproduces the observed radio brightness temperature, rather than just matching the pattern of field lines. In our knowledge, such an FLST model for microwave emission was first implemented by Chiuderi-Drago, Alissandrakis, and Hagyard (1987) in which the electron temperatures are calculated from the heat transfer equations along individual field lines. The nested loop model for microwave emission presented by Klimchuk and Gary (1995) can also be regarded as an FLST model in which temperature and density is correlated with the loop length. In the present study, we consider a set of FLST models in which the temperature per field line depends only on observable quantities at the footpoints of the loop, so that we can determine which observable quantity is the most appropriate by testing the model results against the microwave images.

5.1. Preliminary Check

In Figure 5 we compare several such models with radio observations. In all rows the left-hand panel shows an observed quantity in the photosphere/chromosphere, while the right-hand panel is the projection of this quantity along field lines onto a coronal isogauss surface at 580 G (which corresponds to harmonic $n = 3$ at 4.9 GHz). It is instructive first to discuss these projected quantities, rather than the corresponding radio brightness distributions, in order to understand how each maps into the corona.

In the first row (Fig. 5(a)), we use the optical continuum intensity as a boundary temperature pattern and extrapolate it into the corona along the field lines. Here we are mainly motivated by the fact that the continuum intensity, to the extent that it is described by the Planck function, may be a chromospheric temperature indicator. The high intensity region around S4 is connected to the coronal region where radio emission peaks C1 and X1 occur. The high intensity region around S5 forms a bright lane along N-S, which just lines up with the radio dark lane except that it is hotter rather than cooler than the surroundings. Thus this model agrees with the observed images in the shape of features, but not in the actual temperature pattern. In the second row (Fig. 5(b)) we use the square of the chromospheric velocity measured from the Dopplergram (courtesy of Dr. B. Schmieder, 1996) as an indicator of the kinetic energy of gas. The coronal temperature extrapolated from the Dopplergram signals is similar to that from the continuum, except that it instead predicts a feature lying between S5 and S2, similar to the X2 peak.

In the third row (Fig. 5(c)) we show the total photospheric magnetic field strength, B, and its extrapolation to the corona. B appears to correlate with both the continuum intensity and Doppler signals, and thus possesses some advantages of both those signatures, i.e, enhanced temperature in locations of C1, C2, X1, X2, and X3 (cf. Jiao, McClymont, and Mikić, 1997). In the bottom-most row (Fig. 5(d)) we show the total current density, J, derived from the vector magnetogram. The coronal projection of J is similar to that from B and correlates well with the observed intensity peaks. The overlayed contours in Figure 5d$'$ are the unsigned force-free factor, $|\alpha|$ (ratio of J to B). This quantity is large over a wide region above S5, resembling the C2 peak. It is thus likely that an FLST model based on some combination of $\{B, |\alpha|, J\}$ has the potential to reproduce the radio observations.

5.2. Implementing the Field-Line Structured Temperature Model

To implement the FLST model, we perform field-line tracing from the relevant gyroresonant surfaces (specifically, eight isogauss surfaces at 1500, 1000 , 869, 750, 580, 430, and 348 G) down to the photosphere, and read the relevant quantities (such as J and B) at the footpoints. In the initial models we ignore any dependence of temperature on position along the loop and assume instead that the temperature is uniform along a given field line and proportional to one of the quantities, $\{B, |\alpha|, J\}$ at a footpoint (chosen to be the footpoint closer to the relevant isogauss surface rather than the more distant footpoint). The resulting coronal temperature is set to span a range from 1 MK to 6 MK, the latter being the maximum brightness temperature observed at either frequency.

Figure 6 illustrates how this is implemented in practice. In three panels, we plot three groups of field lines, each of which shares the same connectivity, together with the optical continuum image (in greyscale) and the current density, J (white contours). We mark the positions where the 430 G (square symbols) and 750 G (cross symbols) isogauss surfaces intersect with the field lines drawn. The following points are noteworthy. As with a comparison with soft X-ray images, once certain field lines have been identified as “hot” based on a photospheric quantity, a successful magnetic field model should predict that these field lines pass through the apparent projected positions of observed intensity peaks. This is, however, not a sufficient condition for radio modelling; the field lines must also possess the field strength required for gyroresonance right at the positions of observed radio peaks. Figure 6 shows that this is the case; namely, the field lines rooted in regions showing evidence for, e.g., strong currents at the surface, do indeed pass through the appropriate gyroresonant layers where radio emission is strongest (marked as C1, C2, X1, and X2). Further, the position at which this high temperature is seen at radio frequencies will change depending on the observing frequency since different frequencies have different gyroresonant surfaces, and the model must also reproduce this property. Taking the active region field lines as a whole, this means that any systematic change of field line topology with height should be reflected in the morphologies of radio emission seen at different frequencies. We note that there is a trend of counterclockwise rotation of field line orientation with height in region B (Figure 6(b)) and that this is in good agreement with the differing orientation of the radio intensities observed at 4.9 GHz and 8.4 GHz in this region, i.e., C2 and X2. We note that these extra constraints on an FLST model which must be satisfied to model radio data successfully make this combination a very powerful technique to derive information on magnetic field and temperature.

For calculation of $\tau_n(\nu)$, we need to specify the density as well as the temperature. For this purpose we use the well-known scaling law for quasistatic loops by Rosner, Tucker, and Vaiana (1978). The scaling law permits determination of density at the apex of a given loop with known temperature and loop length. Since we assume that pressure is constant along a loop (a field line), this means that density is also assumed constant along the loop if a model of uniform temperature per loop is employed. In a model where we allow temperature to vary along the loop, then density varies accordingly to keep the pressure constant everywhere on the loop.

6. COMPARISON OF COMPUTED RADIO MAPS WITH OBSERVATIONS

We proceed by calculating the radio emissions (Eqs. [1] & [2]) expected from the specific models for the coronal magnetic field, temperature and density as discussed in the previous two sections. Below we compare the result of calculation of the intensity at 4.9 GHz and 8.4 GHz obtained with six different temperature models with the observations.

6.1. Model 1

We first calculate radio intensity expected from a plane–parallel temperature model (i.e., not an FLST model). We do not expect such a model to match the observations, but it serves to emphasize the role of field-line height in the modelling process. The top rows of Figure 7 show the results obtained with use of $T_e(\vec{x}_n) = 1\times10^6$ K + (280 K km^{-1})$\cdot h(\vec{x}_n)$. A positive temperature gradient is chosen in order to reproduce the fact that the observed brightness temperatures decreases at the edges of the active region where the gyroresonant layers are low in the corona.

A plane-parallel temperature model with a positive gradient emphasizes those points where the gyroresonant layers are highest: thus it produces broad peaks above the S5-S6 region. This result reflects the fact that in the FFF model stronger fields are predicted above S5 due to strong currents, which inflates the gyroresonant surface. The overall agreement of this model with the observation is, however, poor: it predicts the wrong morphology (the observed peaks are elongated N-S while the models predict E-W elongation due to the regions of high angular factor, cf. Fig. 4b), and it always predicts higher brightness at lower frequencies when a positive temperature gradient is used, whereas the maximum microwave intensity observed at 8.4 GHz is actually higher than that at 4.9 GHz. Since the gyroresonant layers emitting at 8.4 GHz must lie lower than those at 4.9 GHz, a negative temperature gradient is needed in order to reconcile with the observed radio intensity values. It is thus likely that the real coronal temperature gradient with height must be positive in some places but negative elsewhere, which a simple plane-parallel temperature model is unable to reproduce.

6.2. Model 2

We now turn to various versions of the FLST. As the first of these, we consider the hypothesis that coronal electron temperature is proportional to the magnetic field strength at the footpoint. This hypothesis is motivated by Jiao, McClymont, and Mikić's (1997) finding that bright soft X-ray loops tend to have relatively strong magnetic fields at their footpoints. Their speculation is that if loops are heated by the photospheric turbulence and topological dissipation (Parker 1972, 1983; Mikić, Schnack and Van Hoven, 1988; Longcope and Strauss, 1994; Gomez, DeLuca, and McClymont, 1995), strong fields can better couple with turbulence to produce more efficient heating in the corona. But such a relationship between field strength and heating would not persist in all ranges of field strengths because strong fields are too rigid to be mechanically influenced by turbulence. Therefore we set a critical field strength, B_1, below which the temperature is proportion to the field strength, and above which the temperature drops in proportion to $|B - B_1|$. In the present modeling, we choose $B_1 = 1600$ G based from the overall agreement of the model calculation with the observation (cf. Jiao, McClymont, and Mikić, 1997).

The results are shown in the second row of Figure 7. This model is much closer to the observation than the plane parallel model (model 1): we see a clear division between regions A and B as in the observed images (bottom row in Fig. 7), the peaks in region A have an orientation consistent with those observed, and the lane of depressed radio emission between spots S1 and S2 is quite similar to that observed at both frequencies. However a weakness of model 2 is that the intensity peaks in region B do not resemble the observed peaks, C2 and X2.

The partial success of model 2 (an FLST model) suggests the following. Both models 1 and 2 assume that the coronal temperature is determined by the influence of the underlying magnetic fields. However model 1 depends only on the field strength (i.e. a scalar property), which changes smoothly across the interface between regions A and B. In terms of the field line connectivity (i.e., a vector property of magnetic fields), however, there is a drastic change across the interface (see Figs. 5a and 5a$'$), which appears in the FLST model as a division between regions A and B, consistent with the radio observations. Using only the magnetic field strength to characterize the fields is, therefore, insufficient to reflect the physical properties of magnetic fields in regions A and B in radio emission models.

6.3. Model 3

Here we set the temperature per field line proportional to the force-free factor, α (which is constant along a field line). This is motivated by the speculation (in Porter and Klimchuck 1995) that energy is released via reconnection or resistive effects at the moment when the twist reaches a critical value. It is then expected that field lines with high α, rather than high field strength, would be hot. The results are shown in the third rows of Figure 7. As expected from the $|\alpha|$ distribution (Fig. 5 d$'$) this model predicts a single, broad bright emission located in region B. This hypothesis, therefore, does not reproduce images in the whole active region. A positive point of the model is, however, that it works well in the region where α is significant. At 4.9 GHz it reproduces the broad area and the N-S orientation of the intensity peak C2; at 8.4 GHz the model predicts intensity at the position of X2 with the correct N-W orientation. In terms of the overall morphology, however, we note that models 2 and model 3 are only partially successful.

6.4. Model 4

We next consider the hypothesis that the temperature in a loop is proportional to the total current density, J, entering the loop and show the result in the top row of Figure 8. This model reproduces the 8.4 GHz image very well. In region B where α is significant, the current density morphology resembles that of α, and thus predicts an intensity peak resembling X2, as in model 3. In region A α is small, but there is still quite a strong current density due to the high field strengths, so that this temperature model is able to reproduce C1 and X1, as in model 2. While this model yields results superior to those of models 1–3, there remain several discrepancies with the observed images. The model intensity at 4.9 GHz at the position of the observed C1 peak is too weak. The maximum intensity in region B is similar in shape to, but not coincident with, C2. The biggest discrepancy is the existence of a bright feature above S1 at both frequencies which has no observed counterpart.

6.5. Model 5

We consider an alternative FLST model in which temperature on a loop varies as a function of arc length from the loop-top. As motivation we note that the unwanted strong source above S1 found in model 4 lies at a relatively low height, whereas the other bright sources lie close to the apex of small loops. Theoretically a coronal loop in quasi-static equilibrium should have highest electron temperature at its top and the temperature elsewhere should decrease with arc length, i.e., the distance along the field line from the loop top (Rosner, Tucker, and Vaiana, 1978; Craig, McClymont, and Underwood, 1978). We note that in Rosner, Tucker, and Vaiana's (1978) model, the temperature variation with arc length l is well approximated by a simple power law: $T_e(l) \sim l^{1/2}$ (their Fig. 11). To incorporate this physics into the present model we use, instead of a uniform temperature model, the form $T_e(l) = T_{\rm base} + T_e^{\rm top}(l/L)^{1/2}$ where l is the arc length measured from the footpoint to the position of gyroresonant point in the loop and L is the half arc length of the loop; $T_e^{\rm top}$ is still determined by the current density, J, at the footpoint.

The maps shown in the second rows of Figure 8 are obtained using such a temperature model. The brightness above S1 at 4.9 GHz is indeed suppressed, leaving an intensity feature elongated N-S in region A and a low intensity lane next to which is more pronounced than in model 4. The model for 8.4 GHz shows peaks with a remarkable resemblance to the observed peaks, X1 and X2. The brightness temperature depression between regions A and B is also more consistent with the observation.

In addition to the morphological similarity between this model and the observations, we note another attraction of this model: the ability to explain the 3D organization of temperature in this active region. A dilemma with the plane-parallel temperature model (model 1) is that a positive temperature gradient is needed to reproduce the radio images at the active region boundary and the relative brightness of C1 and C2, while a negative gradient is needed at the positions of maximum brightness in order to explain why the brightness temperature of X2 is higher than that of C2. A model of utilizing a length-dependent variation of temperature fulfills both requirements simultaneously because long, extended loops originate near the boundary of the region while small loops lie near the magnetic neutral lines where the radio emissions are brighter.

6.6. Model 6

As a final model, we allow for the possibility of an error in the magnetogram on which the extrapolation was based. Model 5 shows that the 4.9 GHz intensity peak in region B lies displaced slightly to the east of the observed peak C2, and the peak distribution is less extended than observed. Also the radio depression between regions A and B predicted by the model at 4.9 GHz is less prominent than that observed. Both these discrepancies will be improved if the real radio source lies at a height greater than the present model predicts: the model C2 peak will shift westwards due to the projection effect; the peak distribution, in general, tends to expand with height; and the depressed lane at 4.9 GHz is likely to be more N-E oriented thanks to the rotation of magnetic field lines with height in this region (Section 4.2).

The actual emission layer could be located higher than we modelled if the photospheric magnetic field measurement were off by a certain amount or if the model fields were insufficiently relaxed to the force-free state. However, it is hard to assess all the possible errors and their consequences for the field extrapolation (see Lee et al. 1997). For the purpose of assessing a possible error range, we here investigate the effects of the arbitrary assumption that magnetic field strength in the whole active region was uniformly underestimated by, say, 30%. We therefore multiply the present magnetic field model by a constant factor of 1.3 and redo the calculations for model 5. The results are shown in the third row of Figure 8. There is obvious improvement in the 4.9 GHz map: the model shows an intensity peak in region B now more extended and shifted westward, closer to the observed source C2 in projection. The depression pattern between C1 and C2 now better matches the observed one in orientation, although in a slightly displaced position. The model at 8.4 GHz now exhibits intensity peaks similar to X1, X2 and even X3 (the only model among those we have tried so far to predict a peak resembling X3).

7. CONCLUSION

In this paper we have explored the magnetic and temperature structure of a complex active region, AR 6615, by comparing coronal temperature models with radio observations at two frequencies. We have employed an FLST model as a more realistic approach for comparison with radio images than most previous analyses. In an FLST approach, modeling of the temperature structure cannot be regarded as distinct from modeling the magnetic field: the two are closely linked. Since we considered only models based on observed quantities, we have minimized the dependence of our results on arbitrary choices of input free parameters.

In this modelling, we have pursued two issues: (1) which magnetic field model is capable of reproducing the radio images? and (2) what physical quantity best correlates with the observed coronal temperature? With regard to (1), only the nonlinear FFF model predicts the field line topology in a form that agrees with what we infer from both the microwave and Hα images. Potential and linear FFF models predict field line connectivity inconsistent with the observed radio as well as Hα morphology.

Regarding (2), our modelling favors the hypothesis that temperature of a loop is determined by the current density entering the loop. This result, $T_e \sim J$, is not readily understandable in terms of existing theories. In Parker's (1972, 1983) theory, coronal heating is produced by small-scale currents existing in the corona in filamentary forms. It is, however, unknown how such small–scale currents are related to the large-scale currents which are sensed by photospheric vector magnetograms (cf. Metcalf et al. 1995). Jiao, McClymont, and Mikić (1997) provided an insight into the connection between photospheric magnetic fields and coronal heating within the framework of Parker's theory by suggesting that the efficiency of the coupling between the photospheric magnetic fields and turbulence increases in proportion to field strength. In our experiment, the hypothesis $T_e \sim B$ yields a result in good agreement with observation especially in regions where α is low. In regions where α is high, however, the hypothesis $T_e \sim J$ seems to work better.

Although we cannot provide a firm interpretation of the result $T_e \sim J$, our speculation at a very superficial level is as follows. By analogy with Jiao, McClymont, and Mikić's (1997) interpretation, we also consider that the efficiency of the interaction between the magnetic fields and turbulence influences heating in the corona and thus the temperature on each loop. That efficiency may well depend on the level of turbulence as well as the field strength. Thus, if the turbulence inside the active region is not evenly distributed in space, but rather is enhanced in some local regions, it is likely that α in those regions tends to be high. Then it would certainly be the case that J rather than B is a better indicator of the coupling between the magnetic fields and turbulence, so that the coronal loop temperature shows a correlation with J in the photosphere. In this sense, our result implies a connection between photospheric magnetic fields, turbulence, and coronal heating as in Parker's theory for coronal heating in active regions (Parker, 1972, 1983).

Acknowledgements

We thank the referee, Dr. J. A. Klimchuk, for his helpful comments and suggestions. This work has been supported by NSF grant ATM-93-16972 and NASA grant NAG-W-1541. Z. M. has been supported by NASA contract NASW-4728 and NSF grant ATM-9320575. A. N. M. has been supported by ATM 93-20575 and ATM 96-13794. We thank Brigitte Schmieder for allowing us to use her data obtained with the Multichannel Double Pass Spectrograph at Tenerife.

References

Alissandrakis, C. E. and Kundu, M. R. 1984, A&A, 139, 271.
Aschwanden, M. J., Lim, J., Gary, D. E., Klimchuk, J. A. 1995, ApJ, 454, 512.
Brosius, J. W., Wilson, R. F., Holman, G. D., and Schmelz, J. T. 1992, ApJ, 386, 347.
Brosius, J. W., Davila, J. M., Thomas, R. J., and White, S. M. 1996, ApJ, 488, 488.
Craig, I. J. D., McClymont, A. N., and Underwood, J. H. 1978, A&A, 70, 1.
Chiuderi-Drago, F., Alissandrakis, C., and Hagyard, M. 1987, Solar Phys., 112, 89.
Gary, D. E. and Hurford, G. J. 1994, ApJ, 420, 903.
Golub, L. 1996, Astrophys. & Space Sci., 237, 33.
Gomez, D. O., DeLuca, E. E., and McClymont, A. N. 1995, ApJ, 448, 954.
Gopalswamy, N., Raulin, J.-P., Kundu, M. R., Hildebrandt, J. Krüger, A., and Hofmann, A. 1996, A&A, 316, L25.
Jiao, L., McClymont, A. N., Mikić, Z. 1997, Solar Phys., 174, 311.
Klimchuk, J. A. and Gary, D. E. 1995, ApJ, 448, 925.
Klimchuk, J. A. and Porter, L. J. 1995, Nature, 377, 131.
Lee, J., White, S. M., Gopalswamy, N., and Kundu, M. R. 1997, Solar Phys., 174, 175.
Longcope, D. W. and Strauss, H. R. 1994, ApJ, 426, 742.
McClymont, A. N., Jiao, L., and Mikić, Z. 1997, Solar Phys., 174, 191.
Melrose, D. B. 1980, Plasma Astrophysics, Gordon and Breach: New York.
Mein, P. 1991, A&A, 248, 669.
Mein, N., Mein, P., Schmieder, B., Engvold, O., Molowny, R., and Ai, G. 1993 in ASP conference Series Vol. 46, Harold Zirin, G. Ai, H. Wang eds.
Metcalf, T. R. 1994, Solar Phys., 155, 235.
Metcalf, T. R., Canfield, R. C., Hudson, H. S., Mickey, D. L., Wulser, J.-P., Martens, P. C. H., Tsuneta, S. 1994, ApJ, 428, 860.
Mikić, Z. and McClymont, A. N. 1994, in *Solar Active Region Evolution: Comparing Models with Observations*, ed. K. S. Balasubramaniam and G. Simon, A.S.P. Conf. Series, 68, 225.
Mikić, Z., Schnack, D. D., and Van Hoven, G. 1988, ApJ, 338, 1148.
Nindos, A., Alissandrakis, C. E., Gelfreikh, G. B., Kundu, M. R., Dere, K. P., Korzhavin, A. N., and Vogod, A. N. 1996, Solar Phys., 166, 55.
Nitta, N. White, S. M., Kundu, M. R., Gopalswamy, N., Holman, G. D., Brosius, J. W., Schmelz, J. T., Saba, J. L. R., and Strong, K. L. 1991, ApJ, 374, 374.

Parker, E. N. 1972, ApJ, 174, 499.
Parker, E. N. 1972, ApJ, 264, 642.
Porter, L. J. and Klimchuk, J. A. 1995, ApJ, 454, 499.
Robinson, P. A. and Melrose, D. B. 1984, Aust. J. Phys. 37, 675.
Rosner, R., Tucker, W. H., and Vaiana, G. S. 1978, ApJ, 220, 643.
Schmahl, E. J., Kundu, M. R., Strong, K. T., Bentley, R. D., Smith, J. B., and Krall, J. R. 1982, Solar Phys., 80, 233.
Schmelz, J. T., Holman, G. D., Brosius, J. W., and Gonzalez, R. D. 1992, ApJ, 399, 733.
Schmelz, J. T., Holman, G. D., Brosius, J. W., and Wilson, R. F. 1995, ApJ, 434, 786.
Vourlidas, A., Bastian, T. S., and Aschwanden, M. J. 1997, ApJ, 489, 403.
White, S. M. and Kundu, M. R. 1997, Solar Phys., 174, 31.
Zheleznyakov, V. V. 1962, Soviet Astron., 6, 3.
Zirin, H. 1988 Astrophysics of the Sun, Cambridge University Press.

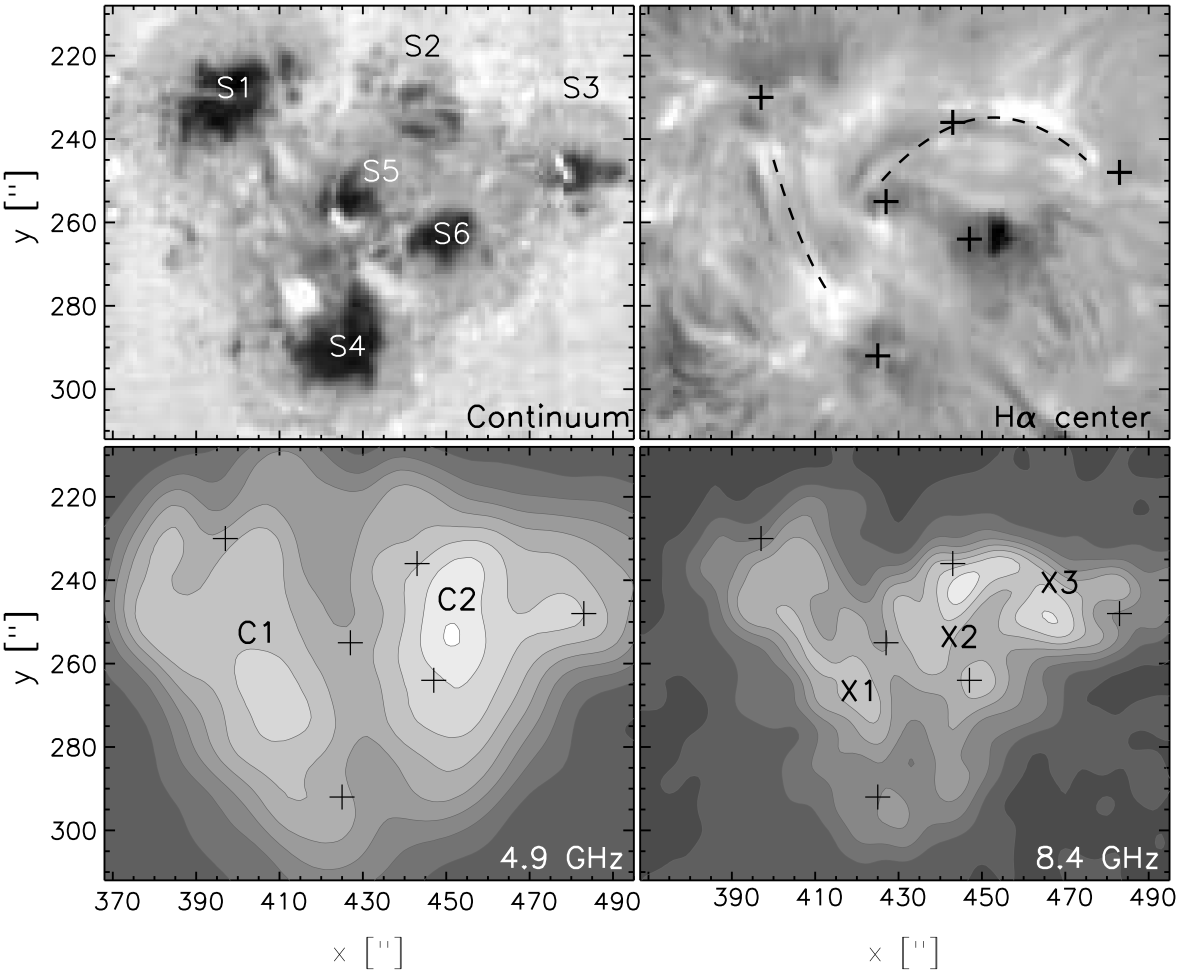

Figure 1. Upper two panels: optical continuum and Hα line center images of AR 6615. Lower two panels: total radio intensities at 4.9 GHz and 8.4 GHz, respectively. In the optical continuum image we name the sunspots as S1–S6 and marked their positions in the other three frames by cross symbols. In the Hα image, two dashed lines are plotted to guide the field line connectivity inferred from the image. C1–C2 and X1–X3 are local maxima of radio intensities at 4.9 GHz and 8.4 GHz, respectively. In this figure and all other figures the (x, y) coordinates are geocentric coordinates in the west and the south, respectively; x and y increase toward the west and the south, respectively.

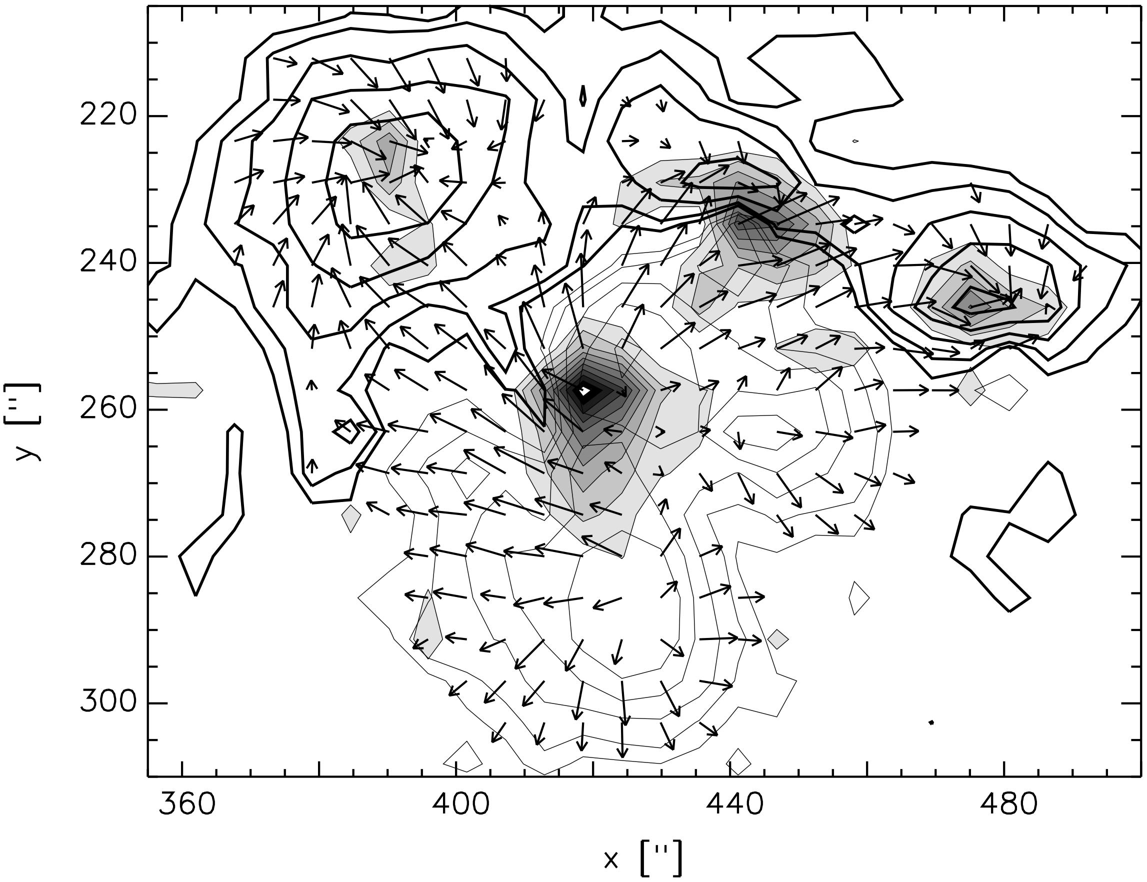

Figure 2. A vector magnetogram of AR 6615 from the Stokes polarimeter at Mees Solar Observatory. The thin and thick contours represent longitudinal fields in the positive and negative polarities, respectively, at levels of ±[150, 300, 600, 1000, 1500] G. Arrows show transverse fields with 180° ambiguity removed. The greyscale images represent magnitude of the longitudinal electric currents calculated from the curl of transverse fields in the range of 4.7 to 16 mA m^{-2}.

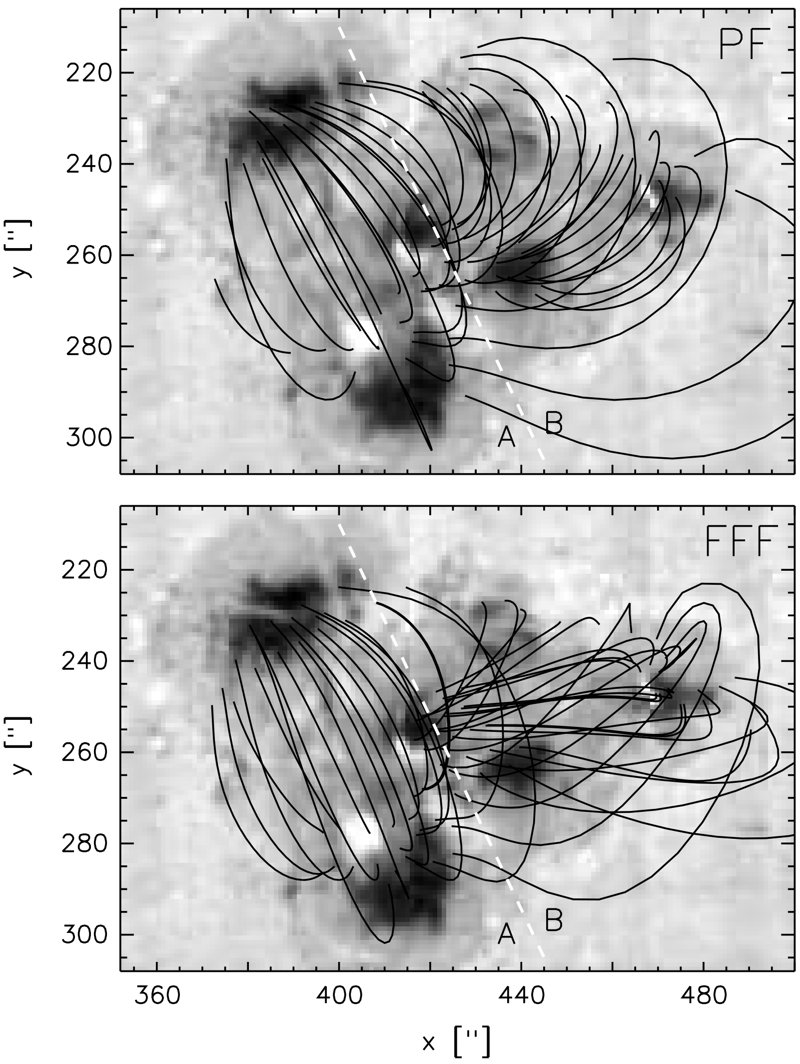

Figure 3. Magnetic field lines of force predicted by the PF (upper panel) and a nonlinear FFF extrapolations (lower panel). The white dashed line distinguishes a potential-like region (region A) and a non-potential region (region B).

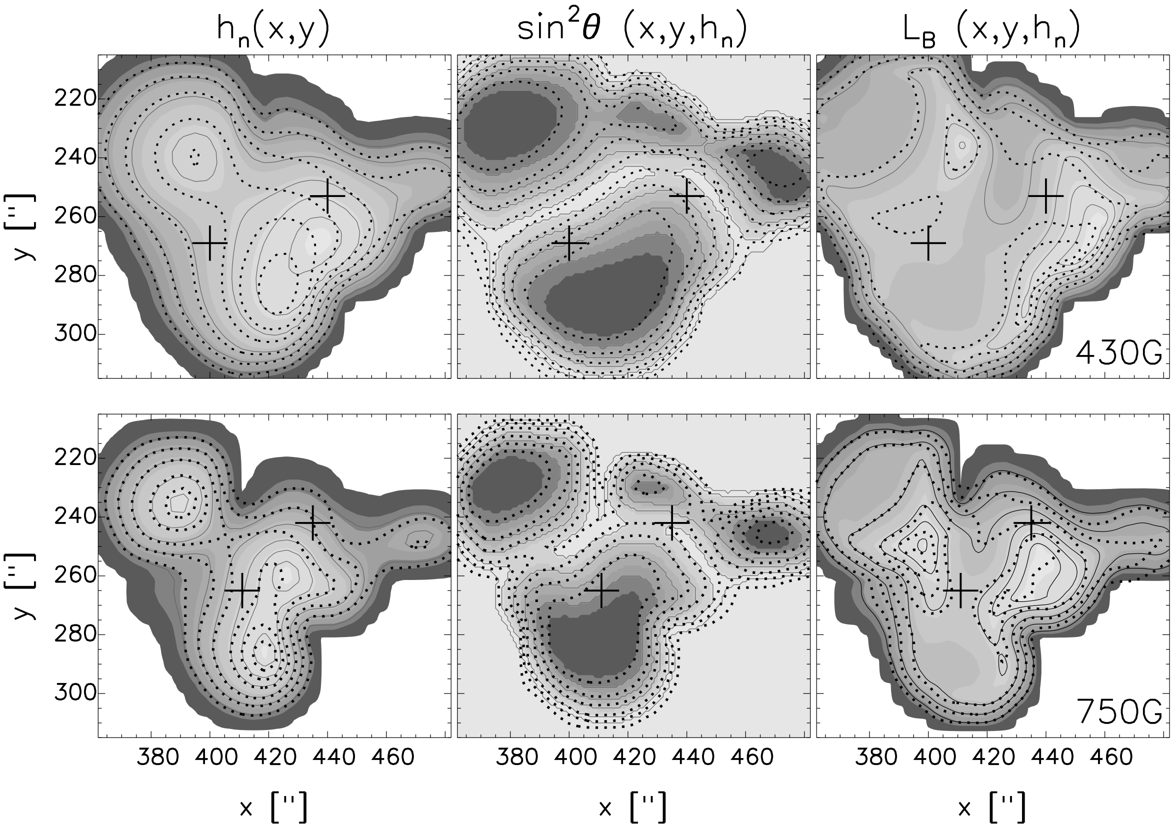

Figure 4. Magnetic parameters for gyroresonant emission at two isogauss surfaces at 430 G (upper panels) and 750 G (lower panels). The first, second and third columns show height of the isogauss surface, h_n, emission angles, $\sin^2\theta$, and magnetic length scale, L_B, respectively. The brighter features have higher values. Scales of these quantities are listed in the text. The cross symbols in the upper three panels represent positions of observed C1 and C2 (see Fig. 1), and those in the lower panels are X1 and X2.

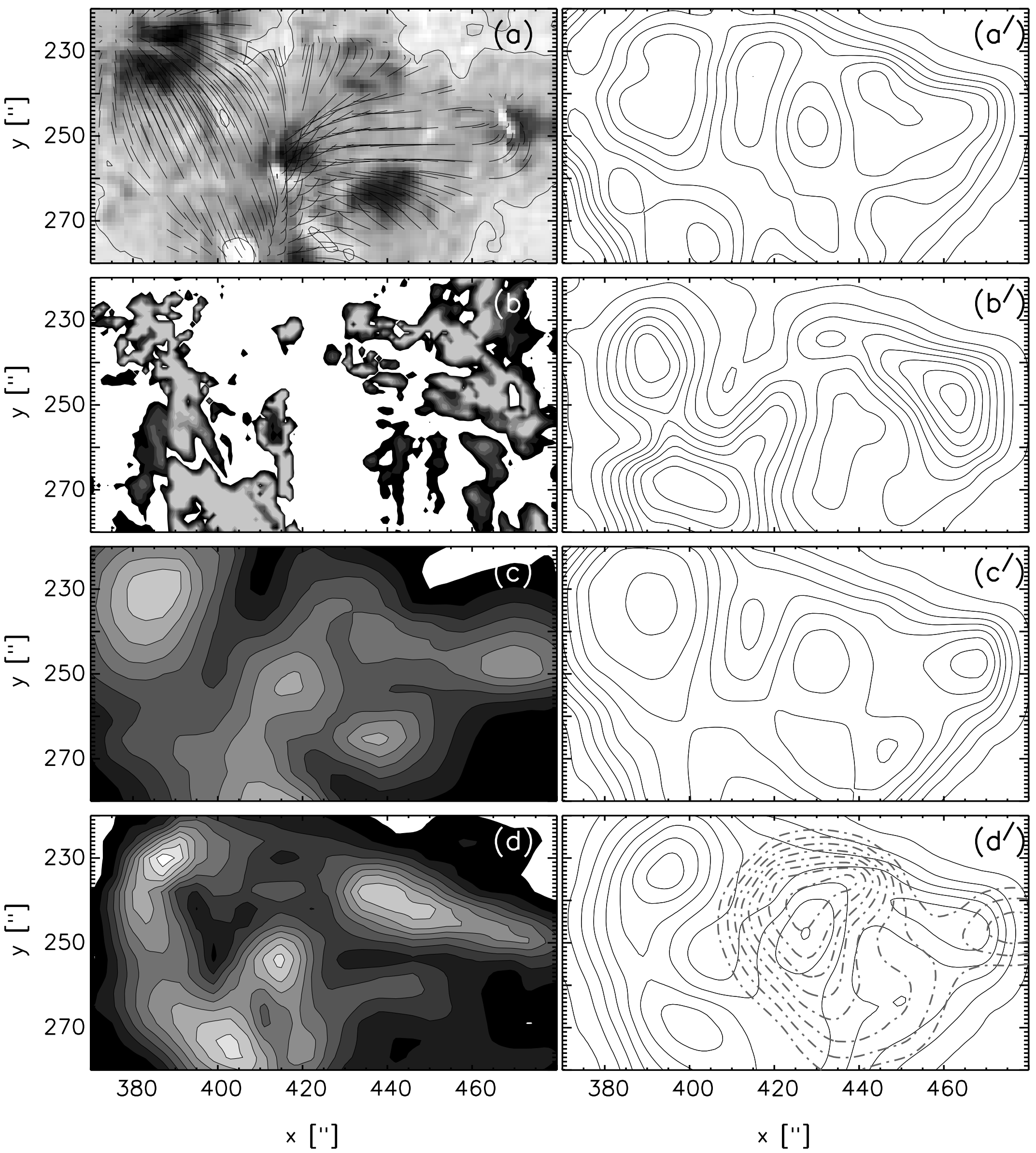

Figure 5. Comparison of the photospheric or chromospheric quantities with their coronal conjugates at the 580 G isogauss surface: (a) optical continuum intensity, (b) square of Dopplergram signals, (c) total magnetic field strength, and (d) total current density. (a′)–(d′) are their coronal conjugates as defined in the text. The dot-dashed contours superimposed in (d′) are the force-free factor, α, in the corona. Field lines connecting these two layers are shown in (a).

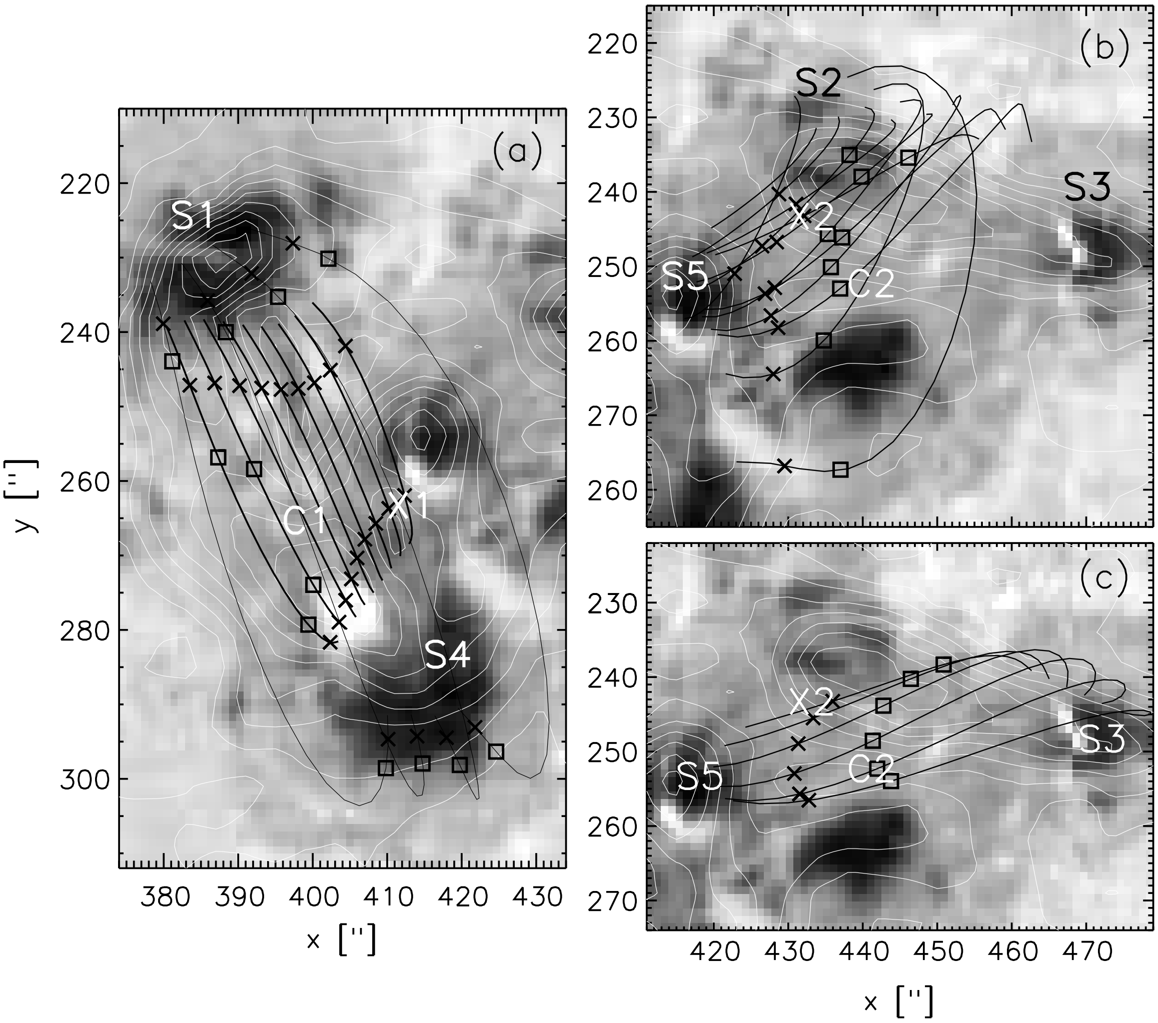

Figure 6. Locations of gyroresonant positions on selected field lines connecting (a) S1–S4, (b) S2–S5, and (c) S3–S5. The positions of the points of 430 G and 750 G are marked by square and cross symbols, respectively. The continuum intensity is shown as background image and white contours represents the total current density.

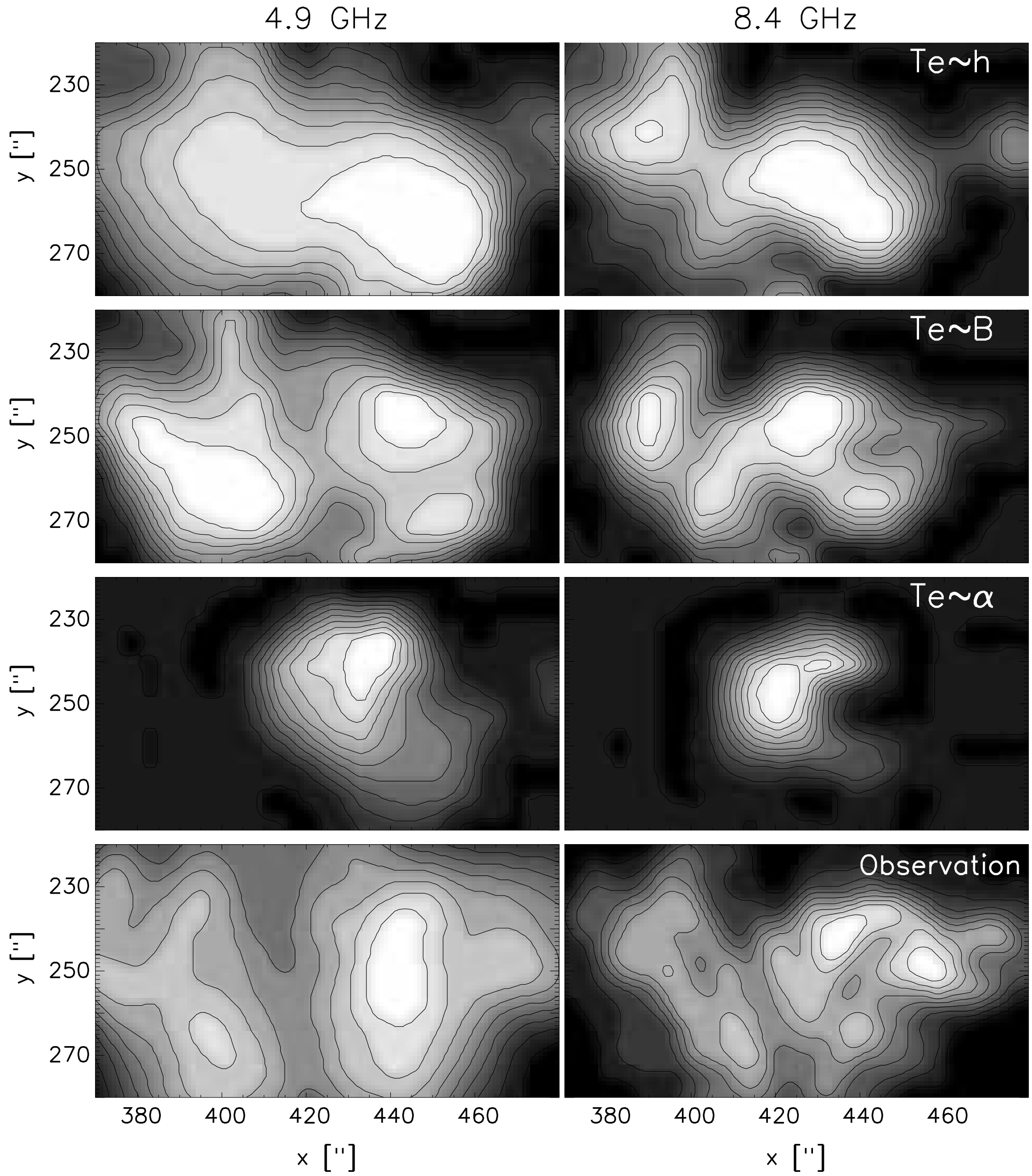

Figure 7. (a)-(d) from top to bottom. Model radio intensities at 4.9 GHz (left panels) and 8.4 GHz (right panels) are shown: (a) model 1, (b) model 2, and (c) model 3. Observed radio intensities are shown in (d) for comparison. The key assumption made in each model is written in the upper-right corner in (a)-(c).

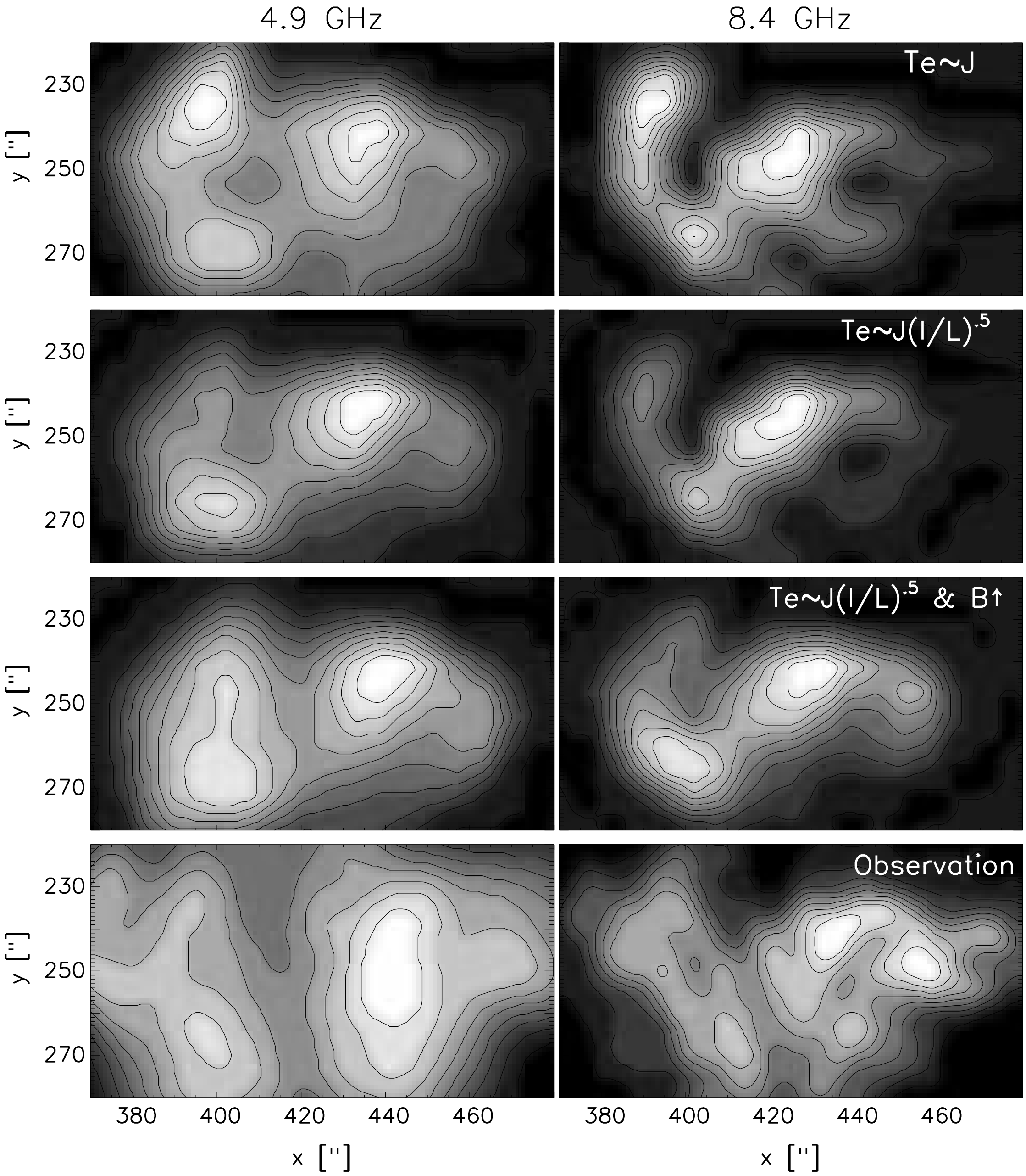

Figure 8. (a)-(d) from top to bottom. Same as Figure 7 for (a) model 4, (b) model 5, (c) model 6, and (d) observed radio intensities.